Performance enhancement of inverted perovskite solar cells through interface engineering by TPD based bidentate self-assembled monolayers

Emre Arkan [a], M. Zeliha Yigit Arkan [a,*], Muhittin Unal [b], Eyup Yalcin [a], Hasan Aydin [c], Cem Celebi [d], Mustafa Can [e], Cem Tozlu [a,**], Serafettin Demic [a,f,***]

[a] Department of Materials Science and Engineering, Izmir Katip Celebi University, Izmir, Turkey
[b] Department of Energy Systems Engineering, Karamanoglu Mehmetbey University, Karaman, Turkey
[c] Department of Materials Science and Engineering, Izmir Institute of Technology, Izmir, Turkey
[d] Department of Physics, Izmir Institute of Technology, Izmir, Turkey
[e] Department of Engineering Sciences, Izmir Katip Celebi University, Izmir, Turkey
[f] Central Research Laboratories, Izmir Katip Celebi University, Izmir, Turkey

ARTICLE INFO

ABSTRACT

Perovskite solar cells (PSCs) have recently appeared as a promising photovoltaic technology and attracted great interest in both photovoltaic industry and academic community. Numerous active researches related to the material processing and operational aspects of device fabrication are under progress since PSCs have a great potential for attaining higher performance compared to that of other solar cell technologies. In particular, interfacial engineering is a crucial issue for obtaining high efficiency in solar cells where perovskite absorber layer is deposited between hole and electron transport layers. In inverted type architecture, PEDOT:PSS is used as both hole transport layer and surface modifier; but unfortunately, this material bears instability due to its acidic nature. Thus, self-assembled monolayers (SAMs) not only are considered as suitable alternative, but also their application is regarded as an efficient and cost effective method to modify electrode surface since it provides a robust and stable surface coverage. In this context, we have employed two novel N,N'-bis(3-methylphenyl)-N,N'-diphenylbenzidine (TPD) based SAM molecules to customize indium tin oxide (ITO) surface in inverted type PSCs. Furthermore, fine-tuning of spacer groups enables us to study device performance depending on molecular structure. This study proposes promising materials for anode interface engineering and provides a feasible approach for production of organic semiconductor based SAMs to achieve high performance PSCs.

1. Introduction

As it was initially reported by Miyasaka and co-workers in 2009, PSCs with optically active methyl-ammonium lead halide perovskites ($CH_3NH_3PbX_3$, X: I, Cl, Br) have attracted a lot of interest due to their non-negligible properties such as long charge carrier diffusion length and lifetime, high absorption coefficient, appropriate bandgaps, inexpensive fabrication and being solution processable [1,2]. Relaying on constituent of atoms or molecules in the structure, perovskites can possess impressive array of exciting features changing from superconductivity to catalytic properties [3,4]. Especially, its application in solar cells, the perovskite solar cells (PSCs), has showed great progress in their

power conversion efficiencies (PCE). Fascinatingly, it improved from 3.85% to 23%, within merely 10 years [2,5,6]. The motivation of studying on PSCs is to fabricate stable, cost effective and highly-efficient PSCs. Therefore, researchers not only have put strong efforts comprising perovskite structure modification, film fabrication optimization and interfacial control but also have utilized various methods for the formation of perovskite crystalline structure such as vapor assisted solution process, one-step solution process as well as two step sequential depositions [7–11]. All these attempts have brought different degrees of crystal quality and surface coverage in perovskite film formation [1]. With all that, usage of ideal selective contact, from organic molecules or metal oxides, is also an effective way to decrease charge recombination

---

* Corresponding author.
** Corresponding author.
*** Corresponding author. Department of Materials Science and Engineering, Izmir Katip Celebi University, Izmir, Turkey.
    E-mail address: yigitmz@gmail.com (M.Z. Yigit Arkan).

losses and to increase the open-circuit voltage (V_{OC}) and PCE [12,13].

Depending on device configurations, PSCs can be categorized into two main groups, namely mesoscopic (uses oxide layer; mainly TiO$_2$) or planar heterojunction (so called; 'regular' (*n-i-p*) and 'inverted' (*p-i-n*)) [13,14]. Compared to the mesoporous TiO$_2$-based PSCs, the planar heterojunction solar cells show superior characteristics. First, its simple device architecture and second, the availability of low temperature processing are the most important examples of respective features, which enable roll-to-roll fabrication [13,15]. Among regular and inverted architectures, the latter has significant advantages because hysteresis problem can be minimized in this configuration specifically with the PCBM electron conductor.

ITO is the most commonly used anode electrode in the inverted PSCs due to its transparency in the visible region, ease of patterning and high electrical conductivity [16–19]. However, its rough surface creates pin holes leading leakage currents and surface states due to dangling bonds on the surface that causes recombination of charge carriers via trapping centers at the interface [20,21]. The work function of ITO is reported to change from 4.5 to 4.7 eV that is much lower than the HOMO level of donor material. This prevents the charge transfer from the active layer to the anode layer that is needed for an ohmic contact without potential barrier [13,14]. Furthermore, V_{OC} strongly depends on interface morphology and matching energy levels at the interface [22]. To obtain higher short circuit current density (J_{SC}) and fill factor (FF), the charge carrier collection must be maximized through tuning energy levels and improving the interface. Therefore, interfacial engineering become a significant factor to overcome discussed drawbacks [23]. Usually, PEDOT:PSS (poly(3,4ethylenedioxylenethiophene):poly(styrenesulfonic acid)) is introduced as buffer layer in inverted PSCs. Unfortunately, since ITO is an acid-sensitive material, the inherent acidic nature of PEDOT:PSS can therefore result in etching of ITO surface [24–26]. Similarly, the polymer layer in device architecture can readily be oxidized in air leading to deterioration in device performance [27].

The application of SAMs is an effective strategy for improving the device efficiency due to their excellent chemical and physical properties [28,29]. A typical SAM molecule is composed of three groups: a head group that has a high affinity to the surface, tail group that determines interfacial properties of the SAMs and the terminal functional groups mainly designed to tune chemical interactions at the interface with perovskite [29]. The modification of ITO anode layer by SAMs changes the surface wettability owing to the binding of functional acidic groups to the –OH terminated surface. In addition, SAM modification provides realignment of work function of ITO because of molecular dipole moments on the surface [23]. The alteration in energy level alignment can influence the charge extraction and recombination at the interfaces [1, 13,14]. These results affect the V_{OC}, FF, and J_{SC}.

In this paper, *N,N'*-bis(3-methylphenyl)-*N,N'*-diphenylbenzidine (TPD) based aromatic SAMs with carboxylic acid anchoring groups have been synthesized to modify ITO surface and to increase charge transport in inverted PSC. The carboxylic acid heads on SAMs were used to form ester bonds with hydroxyl groups available on ITO surface. Two neighboring thiophene rings are preferred as conjugation units owing to their lower delocalization energy with respect to benzene and therefore it can offer much effective conjugation than benzene rings. Moreover, thiophene rings are enriched with hexyl chains in one of the proposed structures to compare the effect of straight and branched spacers on target surface and on device parameters. Yet, no attempts, to our knowledge, have been made to develop inverted type PSCs based on this concept. Therefore, the experimental work presented here provides fresh insight into semiconductor futures for efficient transport of electronic holes without the need of polymer and inorganic metal oxide in inverted PSCs.

2. Materials

Methyl 4-bromobenzoate, 5,5′-dibromo-2,2′-bithiophene, 4-methoxycarbonylphenylboronic acid, [1,1′-bi(diphenylphospino)ferrocene] dichloropalladium(II) (Pd(dppf)Cl$_2$) and poly(3,4-ethylenedioxy thiophene)-poly(styrenesulfonate) (PEDOT:PSS), lead(II) iodide (PbI$_2$) were purchased from Sigma-Aldrich. (5′-Bromo-3,4′-dihexyl-[2,2′-bithiophen]-5-yl) boronic acid and (([1,1′-biphenyl]-4,4′-diylbis(*m*-tolylazanediyl))bis(4,1-phenylene))diboronic acid were supplied from SunaTech Inc. All solvents such as 1,2-dimethoxy ethane (DME), tetrahydrofuran (THF), ethanol, anhydrous N,*N*-dimethylformamide (DMF), anhydrous isopropyl alcohol, toluene, acetone, dimethyl sulfoxide (DMSO) and hydrochloric acid (HCl), potassium hydroxide (KOH) were purchased from Alfa-Aesar. Potassium carbonate (K$_2$CO$_3$) was obtained from Riedel de Haen. Methylammonium iodide (MAI) was obtained from Dysol Inc [6,6].-phenyl-C$_{61}$-butyric acid methyl ester (PC$_{61}$BM) was purchased from Luminescence Technology Corp. (LUMTEC).

Synthesis: All chemicals, solvents, and reagents were used as received from commercial source without further purification. All glassware was oven-dried and all Suzuki-Coupling reactions were performed under inert (N$_2$) environment. (For schematic illustration of synthesis steps, Fig. S1 of Supporting Information can be seen).

3. Synthesis method

3.1. Synthesis of methyl 4-(5′-bromo-[2,2′-bithiophen]-5-yl)benzoate

5,5′-Dibromo-2,2′-bithiophene (250 mg; 0.77 mmol) and (4-(methoxycarbonyl)phenyl)boronic acid (69.4 mg; 0.38 mmol) were dissolved in 20 ml DMF in Schlenk Flask. Pd(dppf)Cl$_2$ (15.5 mg; 0.019 mmol) and K$_2$CO$_3$ (1 mL; 1 M) were added to the mixture after temperature was reached to 50 °C. The reaction mixture was heated to 90 °C and refluxed, under N$_2$, overnight. The reaction was monitored with thin layer chromatography (TLC) to establish completion. The final solution was then extracted with equal volume of CH$_2$Cl$_2$ and distilled water. The organic solvent was evaporated and obtained crude product was purified by column chromatography (SiO$_2$, CH$_2$Cl/n-hexane: 1/1) to afford yellow powder as the desired product. ^{1}H NMR (400 MHz, CDCl$_3$, ppm): δ 8.0–7.98 (d, 2H), 7.85–7.80 (m, 2H), 7.42–7.40-7.38 (t, 1H), 7.25 (s, 2H), 3.86 (s, 3H). (Fig. S2).

3.2. Synthesis of dimethyl 4,4'-(5′,5‴-(([1,1′-biphenyl]-4,4′-diylbis(m-tolylazanediyl))bis(4,1-phenylene))bis(([2,2′-bithiophene]-5′,5-diyl))) dibenzoate

Methyl 4-(5′-bromo-[2,2′-bithiophen]-5-yl)benzoate (250 mg; 0.66 mmol) and (([1,1′-biphenyl]-4,4′-diylbis(*m*-tolylazanediyl))bis(4,1-phenylene))diboronic acid (199 mg; 0.33 mmol) were dissolved in 20 ml DMF in a Schlenk Flask. Pd(dppf)Cl$_2$ (27 mg; 0.03 mmol) and K$_2$CO$_3$ (2 mL; 1 M) were added to the mixture after temperature was reached to 50 °C. The reaction mixture was heated to 90 °C and refluxed, under N$_2$, overnight. The reaction was monitored with TLC to establish completion. The final solution was then extracted with equal volume of CH$_2$Cl$_2$ and distilled water. The organic solvent was evaporated and obtained crude product was purified by column chromatography (SiO$_2$, n-hexane/EtOAc: 5/1) to afford orange powder as the target product.

^{1}H NMR (400 MHz, CDCl$_3$, ppm): δ 8.04–8.02 (d, 4H), 7.65–7.63 (d, 4H), 7.45–7.43 (t, 7H), 7.24–7.08 (m, 19H), 6.98–6.93 (t, 6H), 3.92 (s, 6H), 2.28–2.26 (d, 6H). ^{13}C NMR (400 MHz, CDCl$_3$, ppm): δ 166.69, 147.43, 146.89, 146.22, 139.29, 139.11, 138.24, 134.33, 130.29, 129.18, 129.05, 128.69, 128.61, 127.95, 127.33, 127.24, 126.37, 125.47, 125.29, 125.19, 125.09, 125.04, 124.94, 124.84, 124.73, 124.50, 124.34, 124.21, 124.02, 123.92, 123.85, 123.47, 122.88, 122.65, 122.02, 121.66, 52.15, 31.92, 31.42, 30.29, 30.16, 29.70, 29.37, 29.25, 29.12, 22.70, 21.43, 14.14 (Figs. S3–S4).

3.3. Synthesis of 4,4'-(5',5'''-(([1,1'-biphenyl]-4,4'-diylbis(m-tolylazanediyl))bis(4,1-phenylene))bis([2,2'-bithiophene]-5',5-diyl)) dibenzoic acid (EA59)

Dimethyl 4,4'-(5',5'''-(([1,1'-biphenyl]-4,4'-diylbis(m-tolylazane-diyl))bis(4,1-phenylene))bis(([2,2'-bithiophene]-5',5-diyl)))dibenzoate was dissolved in (1:1, V:V) THF-ethanol mixture in round-bottom flask. KOH solution (1 ml; 1 M) was added to reaction mixture and final solution was refluxed overnight. After all organic solvents were removed under reduced pressure, distilled water (10 ml) and 1 M HCl solution was added to flask until pH of the solution reached to region 3–4. Finally, orange product was precipitated, filtered, washed with distilled water and dried overnight.

^{1}H NMR (400 MHz, DMSO-d_6, ppm): δ 7.89–7.83 (m, 12H), 7.77–7.72 (m, 11H), 7.60–7.55 (m, 5H), 7.27–7.24 (m, 9H), 6.87 (s, 3H), 2.26–2.24 (d, 6H). ^{13}C NMR (400 MHz, DMSO-d_6, ppm): δ 172.45, 172.32, 129.41, 129.07, 127.50, 22.53 (Figs. S5–S6).

3.4. Synthesis of dimethyl 4,4'-(5',5'''-(([1,1'-biphenyl]-4,4'-diylbis(m-tolylazanediyl))bis(4,1-phenylene))bis(3,4'-dihexyl-[2,2'-bithiophene]-5',5-diyl))dibenzoate

Methyl 4-(5'-bromo-3,4'-dihexyl-[2,2'-bithiophen]-5-yl)benzoate (250 mg; 0.54 mmol) and (([1,1'-biphenyl]-4,4'-diylbis(*m*-tolylazane-diyl))bis(4,1-phenylene))diboronic acid (163 mg; 0.27 mmol) were dissolved in 20 ml DMF in a Schlenk Flask. Pd(dppf)Cl$_2$ (22 mg; 0.03 mmol) and K$_2$CO$_3$ (2 mL; 1 M) were added to the mixture after temperature was reached to 50 °C. The reaction mixture was heated to 90 °C and refluxed, under N$_2$, overnight. The reaction was monitored with TLC to establish the completion. The final solution was then extracted with equal volume of CH$_2$Cl$_2$ and distilled water. The organic solvent was evaporated and obtained crude product was purified by column chromatography (SiO$_2$, n-hexane/EtOAc: 5/1) to afford orange powder as the product.

^{1}H NMR (400 MHz, CDCl$_3$, ppm): δ 8.04–8.01 (dd, 10H), 7.65–7.63 (dd, 10H), 7.26–7.05 (m, 16 H), 3.92–3.91 (d, 6H), 2.82–2.78 (t, 8H), 2.59–2.56 (t, 6H), 1.71–1.67 (t, 8H), 1.28–1.27 (d, 24H), 0.88–0.86 (d, 12H).^{13}C NMR (400 MHz, CDCl$_3$, ppm): δ 166.72, 142.89, 140.62, 140.04, 138.28, 135.61, 131.91, 130.24, 128.58, 128.50, 127.59, 127.47, 125.00, 52.12, 31.66, 30.74, 30.57, 29.69, 29.60, 29.27, 29.14, 28.99, 22.62, 22.60, 14.10 (Figs. S7–S8).

3.5. Synthesis of 4,4'-(5',5'''-(([1,1'-biphenyl]-4,4'-diylbis(m-tolylazanediyl))bis(4,1-phenylene))bis (3,4'-dihexyl-[2,2'-bithiophene]-5',5-diyl))dibenzoic acid (EA60)

Dimethyl 4,4'-(5',5'''-(([1,1'-biphenyl]-4,4'-diylbis(*m*-tolylazane-diyl))bis(4,1-phenylene))bis(3,4'-dihexyl-[2,2'-bithiophene]-5',5-diyl)) dibenzoate was dissolved in (1:1, V:V) THF-ethanol mixture in round-bottom flask. KOH solution (2 ml; 1 M) was added to reaction mixture and final solution was refluxed overnight. After all organic solvents were removed under reduced pressure, distilled water (10 ml) and 1 M HCl solution was added to flask until pH of the solution reached to region 3–4. Finally, orange product was precipitated, filtered, washed with distilled water and dried overnight.

^{1}H NMR (400 MHz, DMSO-d_6, ppm): δ 7.84–7.75 (d, 27H), 7.25 (s, 7H), 6.87 (s, 2H), 2.28–2.24 (t, 6H), 1.63 (s, 8H), 1.33 (s, 32H), 0.85–0.81 (t, 12H). ^{13}C NMR (400 MHz, DMSO-d_6, ppm): δ 172.47, 172.34, 129.40, 127.45, 79.62, 72.76, 70.21, 63.50, 60.63, 38.65, 35.76, 31.72, 30.86, 29.45, 29.13, 26.27, 25.46, 22.53, 14.39 (Figs. S9–S10).

4. Device fabrication

Commercially purchased ITO coated glasses were cleaned by an ultrasonic cleaning bath with wet cleaning process (15 min in DI-water, acetone and isopropanol, respectively). After cleaning process, ITO substrates were exposed to UV-ozone treatment for 20 min to activate the ITO surface. SAM molecules (EA-59 and EA-60) were dissolved in toluene (4x10^{-4} M) and kept stirring in an ultrasonic bath at 50 °C for 2 h. Then, activated ITO substrates were immersed in SAM solution and kept overnight in ambient air. After that, ITO substrates were removed and rinsed with toluene to remove residual SAM molecules on ITO surface. Alternatively, PEDOT:PSS was deposited on ITO substrate as hole transport material (HTM) by spin coating at 4500 rpm for 45 s and annealed at 120 °C for 30 min. Finally, all substrates were transferred into the glovebox to complete the rest of the device fabrication.

Perovskite solution was prepared with 460 mg lead iodide (PbI$_2$) and 50 mg methyl ammonium iodide (MAI). PbI$_2$ was dissolved in anhydrous DMF:DMSO mixture with ratio of 920:80 μL. MAI was dissolved in 1 mL of anhydrous isopropyl alcohol. The solutions were kept stirring at least for 2 h. Before deposition, both PbI$_2$ and MAI solutions were filtered with a 0.22 μL PTFE filters. The perovskite layer was deposited by spin coating with two-step deposition method. In the first step, 70 μL of PbI$_2$ was spin-coated at 4000 rpm for 60 s. Just after 60 s. 100 μL of MAI was dripped over the spinning substrate and the substrate was kept spinning for further 30 s. After the formation of the perovskite layer, the substrates were annealed at 100 °C for 10 min. Subsequently, 20 mg of PC$_{61}$BM was dissolved in 1 mL of anhydrous chlorobenzene. The solution was stirred for 2 h. Then, 70 μL of solution was deposited via spin coating at 2000 rpm for 30 s. Finally, 20 nm Ca and then 100 nm of Ag were deposited by thermal evaporation under high vacuum. Surface modification of ITO substrate and device fabrication steps is demonstrated in Fig. 1.

5. Instrumentation and device characterization

^{1}H and ^{13}C NMR (Varian-400 MHz) data were recorded at 25 °C using CDCl$_3$ and DMSO-d_6 as solvents and TMS as an internal standard. Electrochemical behavior of SAM-modified ITO substrates was determined by CH Instrument CH440b potentiostat. The surface morphology of bare-ITO and SAM-modified ITO substrates was characterized by Nanosurf Easyscan-2 controller atomic force microscopy (AFM). During KPFM measurements, tin conducting cantilevers were used to obtain the change in the surface potential and work function of the ITO surfaces before and after modification. KSV Attension Theta Lite Optical Tensiometer was used for static contact angle measurements by dispensing a water droplet with average volume of 4 μL. Chemical composition of SAM-modified ITO surface was analyzed with K-Alpha™$^+$ X-ray Photoelectron Spectrometer (XPS) System. X-RAY diffraction (XRD) pattern of perovskite was recorded with Rigaku D/Max-2500 diffractometer using Cu Kα radiation (λ = 1.54 Å). ZeissEvo model SEM was used to obtain surface image of perovskite films. The J-V measurements were performed by using a solar simulator (ABET 11000) and a source meter (Keithley 2400). The curves were registered under 1-sun conditions (100 mW/cm^2, AM 1.5G, reverse voltage scan direction at a speed of 40 mVs^{-1}) calibrated with a silicon photodiode (NREL). The active area of the devices was 0.07 cm^2. The external quantum efficiency (EQE) spectrum was measured through Stanford SR803 lock-in amplifier under monochromatic illumination.

6. Result and discussion

In this study, two SAM molecules with straight and branched spacers were employed. The chemical structure of SAMs and inverted device architecture were indicated in Fig. 2. As stated in the literature, ideal surface modification of ITO is important parameter to closely match the energy level alignment of the ITO/MAPbI$_3$ interface because reduction in energy barrier between work function (WF) of ITO and HOMO level of MAPbI$_3$ is essential for increasing efficient hole collection [13,14]. Similarly, molecular structure of SAMs and effect of their chain variation are important factors to reach ideal surface modification because it
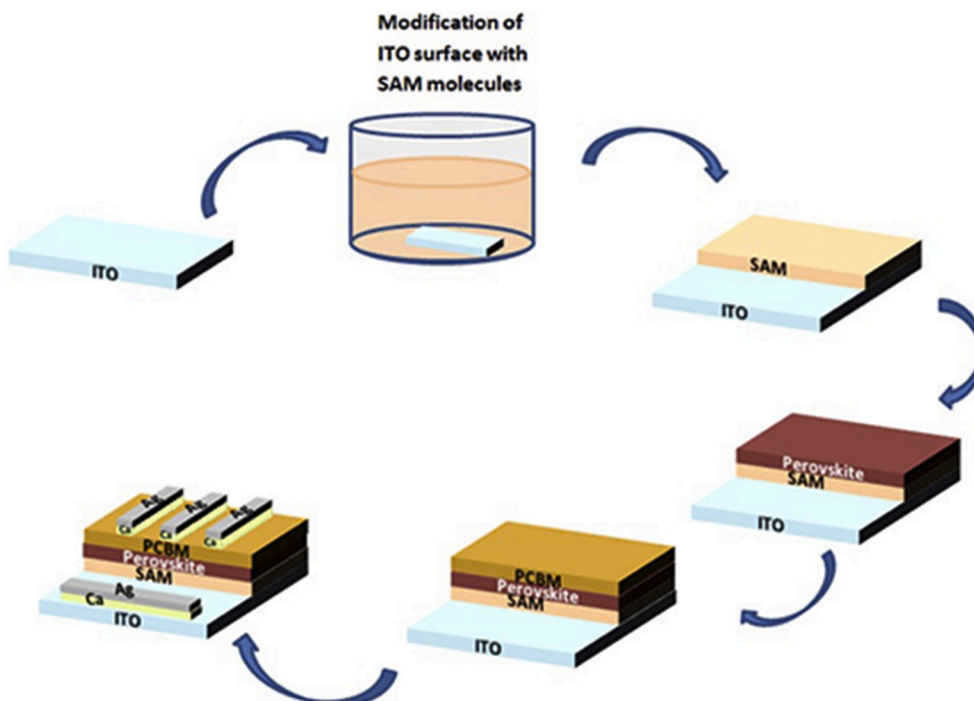
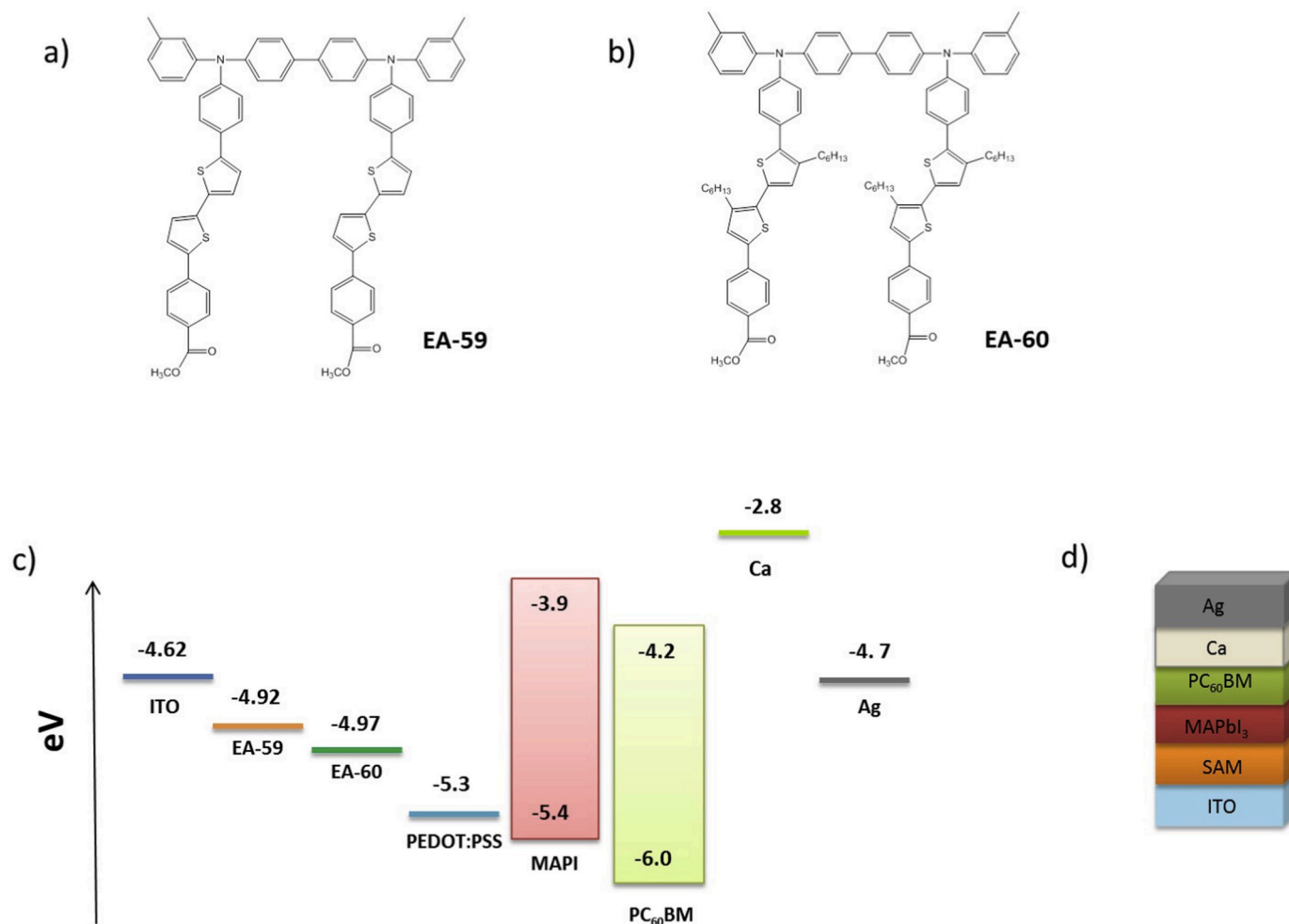**Fig. 1.** Surface modification and device fabrication steps.

Fig. 2. The molecular structure of SAM molecules (a, b). Energy levels of PSC materials employed in this study (c). Layered structure of SAM based devices (d).

determines the interfacial properties [30]. Therefore, proposed SAMs are preferentially synthesized to assess their correlation in device performance.

To evaluate the alteration in WF of ITO electrode before and after SAMs treatment, Kelvin-Probe Force Microscopy (KPFM) measurement was carried out. The bare-ITO displays WF value of 4.62 eV and WF values of ITO after SAMs treatment was determined as 4.92 and 4.97 eV for EA-59 and EA-60, respectively (Fig. S11). From the point of view of energy level alignment of electronic states, convenient photo-carrier collection at anode side is expected to bear closer WF of ITO whilst having lower energy level than HOMO of MAPbI$_3$ [31]. The KPFM results have illustrated that though both SAMs treatment caused favorable WF increase, EA-59 is more promising in terms of hole collection with respect to EA-60.

Electrochemical features of SAM treated ITO has provided further insight into efficiency of SAM molecules on electrode surface. As can be seen in voltammograms (Fig. S12), surface grafted ITO electrodes have inflection points at 0.90 and 0.94 eV for EA-59 and EA-60, respectively. It is worth to note in here that consistent with previous findings, this result may be explained by the fact that branched and long hydrocarbon chain of EA-60 leads to more dominant steric effect and hinders further SAM reaction that results in remaining great amount of hydroxyl group without substitution and significantly enhanced heterogeneity on target surface [30]. This is a possible explanation 0.04 eV differences in inflection point between EA-59 and EA-60 modified ITO electrodes. Moreover, this result also broadly supports CPD (contact potential difference) values obtained from KPFM graphs and clarifies why EA-59 treated ITO surface has the lower WF alignment with respect to EA-60 treated ITO electrode.

Further exploration to evaluate surface modification of SAM molecules has been achieved by examining the contact angle and topographical images of ITO surface. So, sessile water droplet experiment was performed to observe differences in contact angle values of bare and customized ITO electrodes. It is well known that ITO surface is of

hydrophilic properties. The results, as shown in Fig. 3, indicate that SAM grafted ITO surfaces have turned in hydrophobic and EA-59 modified surface shows the higher hydrophobicity than EA-60 modified surface. In addition to surface wettability, surface topography and roughness are simultaneously examined since these parameters are related to wetting characteristic of specimen surface. According to general explanation, if the specimen surface has rough texture on itself, it becomes even more hydrophobic after introduction of chemically hydrophobic molecules [32]. As depicted in Table 1, root-mean-square (RMS) values of ITO surfaces are increased after surface modification by SAM molecules because of agglomeration and creation of extra layer [33]. This surface roughness values and their association with contact angle measurements once again bear out that ITO surface are covered by SAM molecules.

The surface chemical composition of modified ITO electrodes coated with EA-59 and EA-60 SAM molecules were analyzed by XPS. Fig. 4 shows the high resolution survey spectrum of C1s and O1s to analyze the atomic bonds formed on ITO surface for ITO/EA-59 and ITO/EA-60. C1s spectra are fitted by three peaks corresponding to carbon in different chemical environment. The binding energy peaks of C1s for ITO/EA-59 at 285.65, 286.23, 289.18 eV and for ITO/EA-60 at 285.57, 286.13 and 288.85 eV are assigned to C—C/C—H, C—O—C and O—C═O, respectively. The peaks, assigned to O—C═O (ester bonding), at 289.18 and 288.85 eV indicates the formation of covalent bonds between —COOH

Table 1
Comparison of bare and modified ITO surface properties with different techniques.

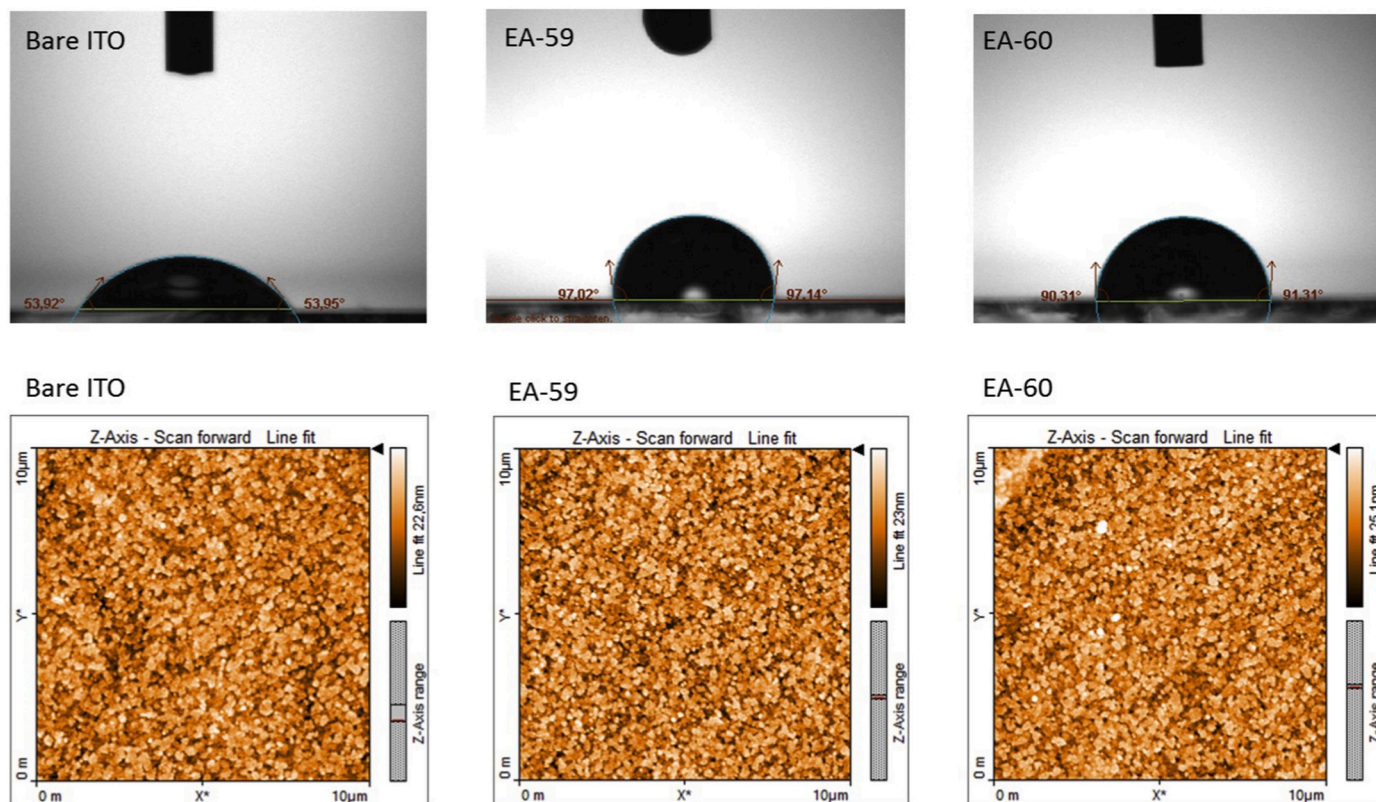| Samples	Oxidation Potentials (V)	Work Functions (eV)	Contact Angles (°)	RMS (nm)
Bare ITO	–	−4.62	53.94	3.73
EA-59	0.90	−4.92	97.08	4.16
EA-60	0.94	−4.97	90.81	4.53

Fig. 3. Topographical AFM images and changes in water contact angle with regard to bare and different SAM coated ITO substrates.
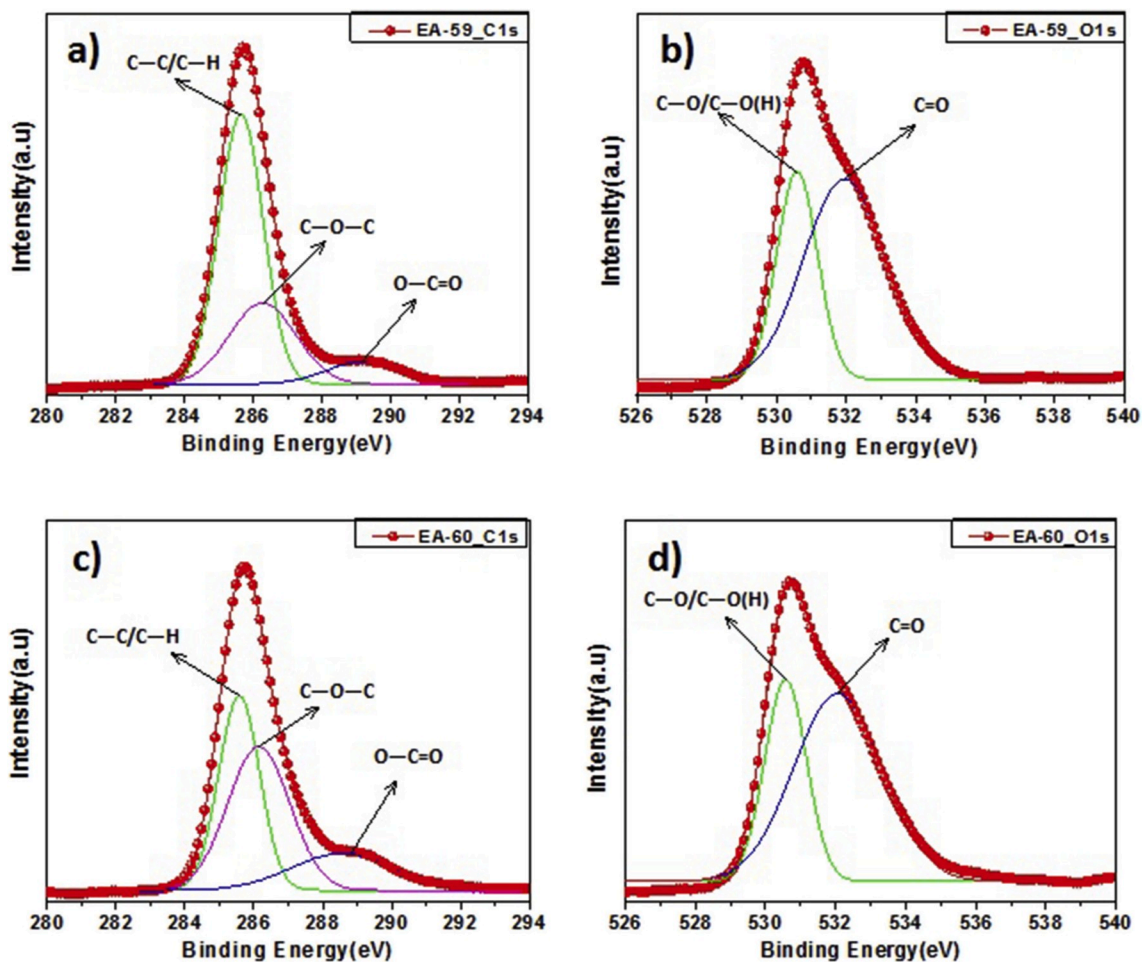
Fig. 4. The XPS high resolution survey spectrum of C1s (a, c) and O1s (b, d) for ITO/EA-59 and ITO/EA-60.

(carboxylic acid) head group of EA-59 (Fig. 4a) and EA-60 (Fig. 4c) molecules and ─OH (hydroxyl groups) existent on the ITO surface [13, 34,35].

O1s high resolution survey spectrum shows two main components for ITO/EA-59 (Fig. 4b). The O1s of ITO/EA-59 peaks observed at 530.57 eV and 531.96 eV are associated with lattice oxide in $ln_xSn_yO_z$ (C–O/C–O(H)) and carboxyl group (C═O), respectively. Approximately the same peaks are obtained from ITO/EA-60 coated surface with values of 530.53 and 532.09 eV (Fig. 4d). The high-resolution survey spectra of N1s and S2p were shown in Fig. S13. Corresponding binding energies of functional groups for ITO/EA-59 and ITO/EA-60 are listed as in Table 2 [36,37].

Fig. S14 shows the wide survey spectrum of ITO/EA-59 and ITO/EA-60. Almost at the same binding energies for C, O, N, S, In and Sn elements are identified on these two ITO/SAM surfaces by XPS. The binding energies at ~486 and ~487 ev, respectively indicates the $Sn3d_{5/2}$ and $Sn3d_{3/2}$ while the peaks at ~445 and ~454 eV confirm the $ln3d_{5/2}$ and $ln3d_{3/2}$, respectively. In addition, the binding energies at ~165, ~286, ~399 and ~531 eV are attributed to S2p, C1s, N1s and O1s elements, respectively [38–40].

The XPS measurements were also performed for bare ITO before treatment with SAM molecules. (Fig. S15). In this measurement, the absence of 'N' and 'S' confirms ITO substrates successfully covered by SAM molecules.

As shown in Fig. 5, XRD is used to characterize the structure of $CH_3NH_3PbI_3$ perovskite. The diffraction peaks at 14.22, 20.15, 23.63, 24.64, 28.59, 30.31, 32.03 and 40,82^0 corresponds to (110), (112), (211), (202), (220), (213), (222) and (224) planes of tetragonal phase of $CH_3NH_3PbI_3$ perovskite, respectively [41–43]. The diffraction peak appearing at 12.83^0 belongs to the residual PbI_2(*) [44,45]. Moreover, diffraction peaks at 38.970, 39.870, 42.950 and 43.500 are relevant to PbI2-MAI-DMF intermediate phase (◆) [45].

The quality of the perovskite film has a crucial effect on performance of PSCs. The film quality is determined by grain size, crystallinity, surface coverage etc. Fig. 6 shows the morphology of the perovskite films deposited on bare ITO (a), ITO/PEDOT:PSS (b), ITO/EA-59 (c) and ITO/EA-60 (d). It is clear from these images that, after the modification of ITO with PEDOT:PSS and SAM molecules, bigger grain size, pinhole-free, high compact and full surface coverage films (which is desirable for PSCs) have been obtained.

Table 2
The corresponding bonding energy of functional groups for ITO/EA-59 and ITO/EA-60.

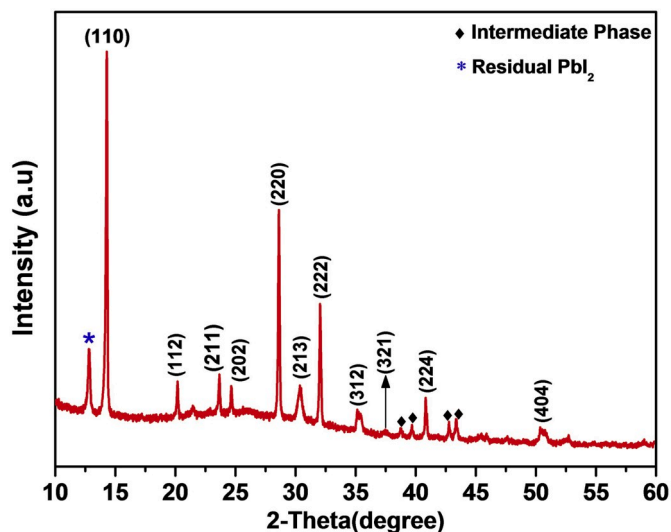| Samples	O1s (eV)		C1s (eV)			N1s (eV)	S2p (eV)
	C–O/C─ (H)	C=O	C–C/C–H	C–O–C	O–C=O		
ITO/EA-59	530.57	531.96	285.65	286.23	289.18	400.30	164.98
ITO/EA-60	530.53	532.09	285.57	286.13	288.85	400.69	164.92

Fig. 5. XRD pattern of CH$_3$NH$_3$PbI$_3$ perovskite film.

6.1. Solar cell performance

Interfacial engineering plays crucial role in PSC because it changes energy level alignment and therefore directly influences the charge extraction and recombination at interface. This situation significantly changes device parameters, namely V$_{OC}$, J$_{SC}$ and FF. Besides that, metal oxide surface possesses many dangling bonds and some active groups covering hydrogen, hydroxyl and carboxyl groups leading to creation of surface trap states that enhance rate of charge recombination [23,46].

Current-voltage characteristics of fabricated solar cells are indicated in Fig. 7 and obtained device parameters are depicted in Table 3. Different from SAMs, PEDOT:PSS coating has been implemented as a reference cell. The highest efficiency has been attained with EA-59 modification due to convenient energy level and it has performed much better particularly in terms of V$_{OC}$ and FF while J$_{SC}$ value is slightly higher with respect to reference cell that led to 11%

improvement in device efficiency. Moreover, EA-60 modification gave rise to slightly higher J$_{SC}$, but lower V$_{OC}$ and comparable efficiency as against to reference cell. It should be noted that EA-60 has drawback in comparison with EA-59 in terms of surface modification due to its branched and long hydrocarbon chains that might cause more dominant steric hindrance and enhance heterogeneity on ITO substrate [30]. The statement posed in here is also confirmed by contact angle measurements (Fig. 3). The lower contact angle value of EA-60 with respect to EA-59 is an indication of more irregularity in molecular uniformity and remaining of higher amount of unsubstituted active sites on ITO surface. In addition, previous studies have found that defects in SAM layers can leave active surface sites that can readily react with other atoms and molecules, especially metal halide precursors can penetrate flaws such as pinholes and form strong metal-oxide bond [47–49]. Specific example is the electrodeposition of Pb on ITO surface in spite of having been covered by organophosphonic acid monolayer [49]. Recent studies has depicted that preferential deposition of Pb was occurred on monolayer covered polycrystalline ITO due to its higher amount of defect sites [47, 49,50]. Within the framework of this information, it is also expected that our initial treatment of PbI$_2$ precursor on ITO/SAM surface, during the fabrication of perovskite film, can result in the settlement of lead ions on defect sites of ITO/SAM surface and led to the formation of deep trap states where nonradiative recombination can take place that adversely affect the dark-current and built-in potential [51–53]. The value of built-in voltage (V$_{bi}$) can be estimated by extrapolating the linear parts of the J-V curves at J = 0 under dark condition. As depicted in Table- 3, EA-60 modification has performed at lower built-in potential than EA-59, showing that EA-60 modification might increase the formation of possible defect sites at ITO/SAM interface as against to EA-59 and thereby PSC with EA-60 SAM molecule might be subjected to more nonradiative recombination, which has lowered V$_{OC}$ and device efficiency. Therefore, it can be deduced that alteration in device performance may be independently relevant to changes in interfacial optoelectronic characteristics of PSCs.

To have deeper understanding of the effect of SAM modification on device performance, their effect on hysteresis was examined. It can be expected that trap states cause long existing charge carriers and therefore decrease the response speed of device [1,23,54]. Consequently, the
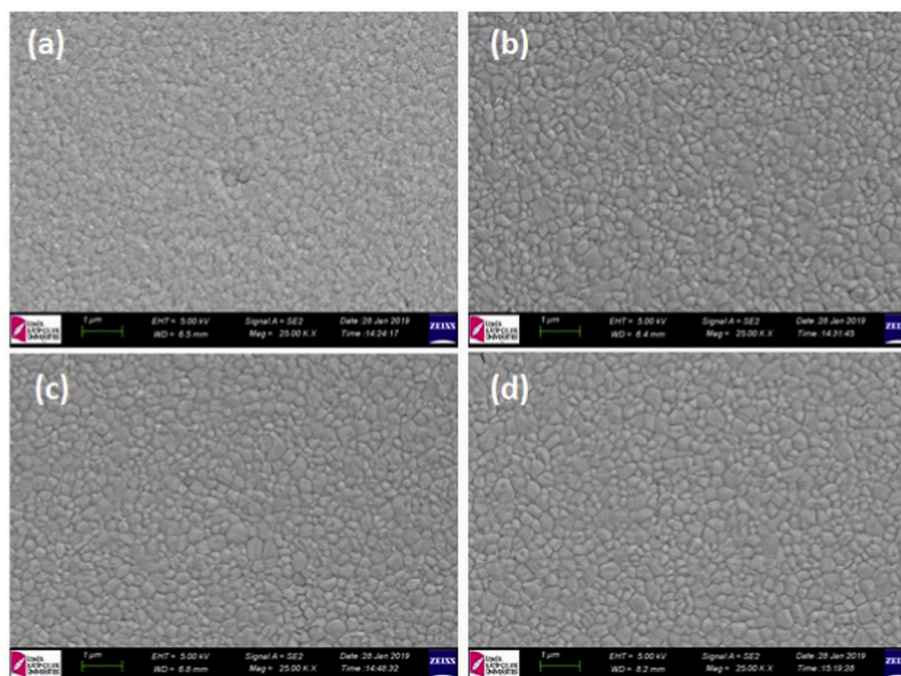

Fig. 6. SEM images of perovskite film deposited on bare ITO (a), ITO/PEDOT:PSS (b), ITO/EA-59 (c) and ITO/EA-60 (d).
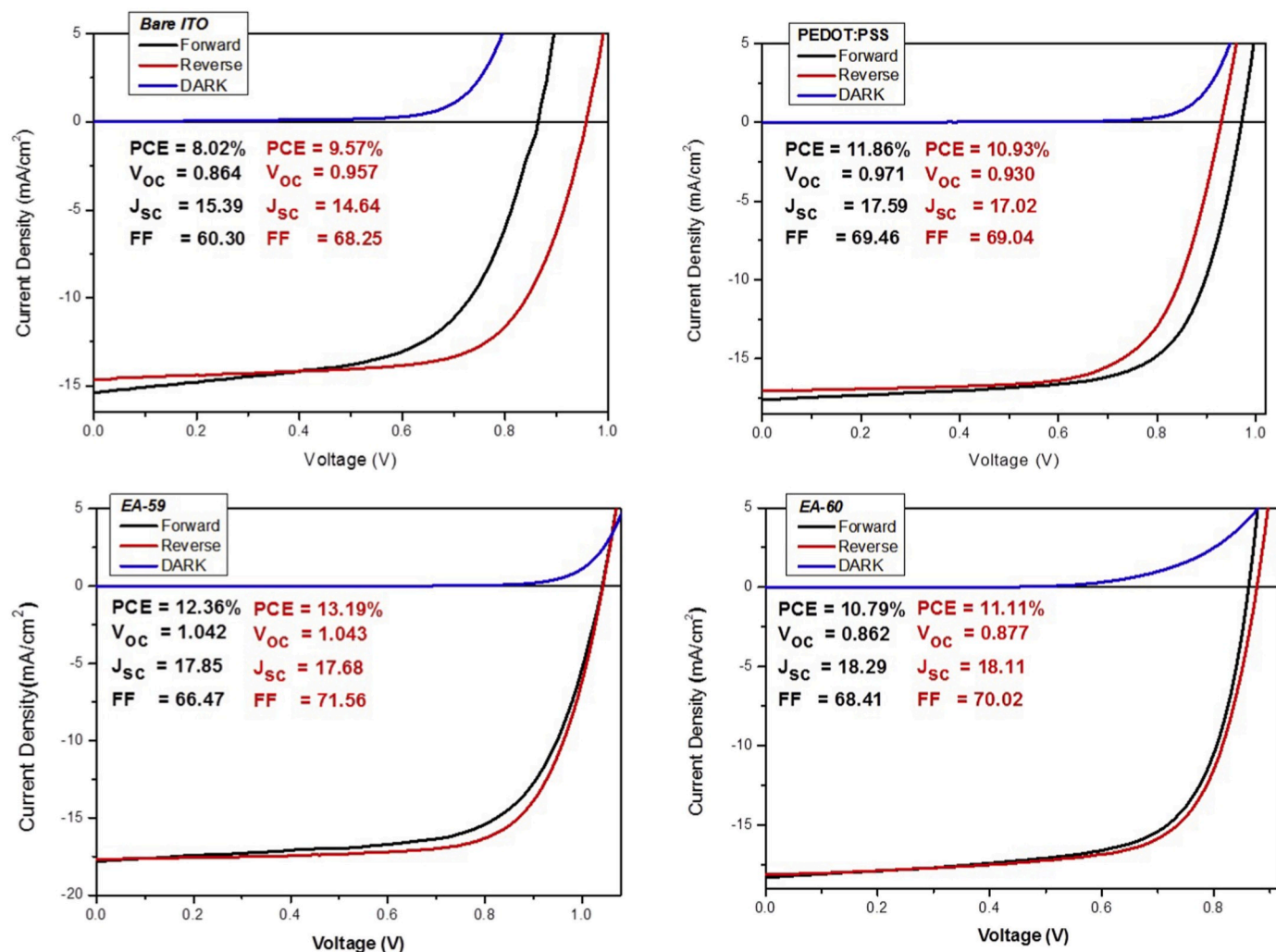
Fig. 7. Current-Voltage characteristics of SAM modified and non-modified devices.

Table 3
Photovoltaic parameters of devices.

Samples	V_{OC} (V)		V_{bi} (V)	J_{SC} (mA/cm^2)			FF		PCE (%)	
	forward	reverse		forward	reverse	integrated	forward	reverse	forward	reverse
Bare ITO	0.864	0.957	0.89	15.39	14.64	15.53	60.30	68.25	8.02	9.57
PEDOT:PSS	0.971	0.930	0.94	17.59	17.02	16.44	69.46	69.04	11.86	10.93
EA-59	1.042	1.043	1.09	17.85	17.68	17.98	66.47	71.56	12.36	13.19
EA-60	0.862	0.877	0.85	18.29	18.11	18.28	68.41	70.02	10.79	11.11

lowered hysteresis can be originated from surface passivation of ITO electrode. As can be seen in current-voltage curves, SAM treatment has fulfilled this necessity and has presented negligible hysteresis compare to reference cell, suggesting that there are efficient charge transfers due to decreased trap density in inverted PSCs.

EQE of PSCs is depicted in Fig. 8. The highest peaks of SAM treated devices have achieved to ~79% and ~80% for EA-59 and EA-60, respectively and they have stronger response than PEDOT:PSS in the wavelength region between 350 and 750 nm. This could be stemmed from optimal chemical interaction at interface that led to better charge extraction and recombination reduction [14,55]. The integrated J_{SC} values are found, in turn, as 17.98 and 18.28 mA/cm^2 for EA-59 and EA-60 that are in agreement with J_{SC} values indicated in I–V measurements (Table 3).

7. Conclusion

In summary, synthesis and interfacial modification of two novel SAM molecules are reported as efficient alternative to PEDOT:PSS to enhance solar cell parameters. Immobilization of SAM on the ITO surface is illustrated as effective method to tune the work function and decrease energy level between ITO and perovskite layer. The spacer groups in aromatic structure is branched with hexyl chain in EA-60 because there have been no published controlled studies, which compare influence of variation of spacers on ITO modification and on device performance. The highest performance has been achieved by EA-59 due to proper energy level arrangement and has indicated 11% improvement in device efficiency with regard to reference cell. EA-60 has shown comparable performance with respect to reference cell and can be considered as rival compound to PEDOT:PSS. The proposed SAM molecules provide simple
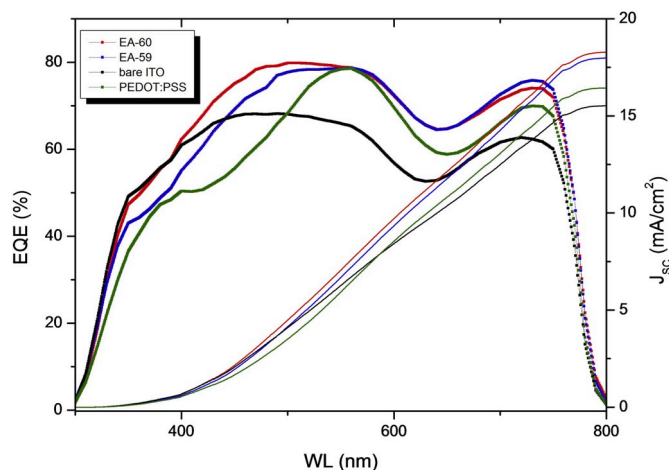
Fig. 8. EQE measurements of devices.

deposition method via solution processes and able to form strong covalent bonds with ITO as well as indicate obvious facility to ensure contact selectivity and decrease charge losses. As revealed in this study, present results will generate fresh platform to design new methodologies as an alternative to inorganic metal oxides and conventional polymers to be applied on acid sensitive surface for the fabrication of high performance and low cost solar cells.

Declaration of competing interest

The authors declare that they have no known competing financial interests or personal relationships that could have appeared to influence the work reported in this paper.

CRediT authorship contribution statement

Emre Arkan: Formal analysis. **M. Zeliha Yigit Arkan:** Supervision, Writing - review & editing. **Muhittin Unal:** Formal analysis. **Eyup Yalcin:** Formal analysis. **Hasan Aydin:** Formal analysis. **Cem Celebi:** Formal analysis, Data curation. **Mustafa Can:** Conceptualization, Data curation. **Cem Tozlu:** Supervision, Writing - review & editing. **Serafettin Demic:** Supervision, Writing - review & editing.

Appendix A. Supplementary data

Supplementary data to this article can be found online at https://doi.org/10.1016/j.optmat.2020.109910.

References

[1] B. Li, Y. Chen, Z. Liang, D. Gao, W. Huang, Interfacial engineering by using self-assembled monolayer in mesoporous perovskite solar cell, RSC Adv. 5 (2015) 94290–94295.

[2] A. Kojima, K. Teshima, Y. Shirai, T. Miyasaka, Organometal halide perovskites as visible-light sensitizers for photovoltaic cells, J. Am. Chem. Soc. 131 (2009) 6050–6051.

[3] J. Coey, M. Viret, S. Von Molnar, Mixed-valence manganites, Adv. Phys. 48 (1999) 167–293.

[4] A. Kulkarni, F. Ciacchi, S. Giddey, C. Munnings, S. Badwal, J. Kimpton, D. Fini, Mixed ionic electronic conducting perovskite anode for direct carbon fuel cells, Int. J. Hydrogen Energy 37 (2012) 19092–19102.

[5] W.S. Yang, J.H. Noh, N.J. Jeon, Y.C. Kim, S. Ryu, J. Seo, S.I. Seok, High-performance photovoltaic perovskite layers fabricated through intramolecular exchange, Science 348 (2015) 1234–1237.

[6] I. Dharmadasa, Y. Rahaq, A. Alam, Perovskite solar cells: short lifetime and hysteresis behaviour of current–voltage characteristics, J. Mater. Sci. Mater. Electron. (2019) 1–9.

[7] S.R. Raga, M.-C. Jung, M.V. Lee, M.R. Leyden, Y. Kato, Y. Qi, Influence of air annealing on high efficiency planar structure perovskite solar cells, Chem. Mater. 27 (2015) 1597–1603.

[8] M.J. Carnie, C. Charbonneau, M.L. Davies, J. Troughton, T.M. Watson, K. Wojciechowski, H. Snaith, D.A. Worsley, A one-step low temperature processing route for organolead halide perovskite solar cells, Chem. Commun. 49 (2013) 7893–7895.

[9] J.-H. Im, I.-H. Jang, N. Pellet, M. Grätzel, N.-G. Park, Growth of CH 3 NH 3 PbI 3 cuboids with controlled size for high-efficiency perovskite solar cells, Nat. Nanotechnol. 9 (2014) 927.

[10] C.-H. Chiang, Z.-L. Tseng, C.-G. Wu, Planar heterojunction perovskite/PC 71 BM solar cells with enhanced open-circuit voltage via a (2/1)-step spin-coating process, J. Mater. Chem. 2 (2014) 15897–15903.

[11] M. Liu, M.B. Johnston, H.J. Snaith, Efficient planar heterojunction perovskite solar cells by vapour deposition, Nature 501 (2013) 395.

[12] S. Ameen, M.A. Rub, S.A. Kosa, K.A. Alamry, M.S. Akhtar, H.S. Shin, H.K. Seo, A. M. Asiri, M.K. Nazeeruddin, Perovskite solar cells: influence of hole transporting materials on power conversion efficiency, ChemSusChem 9 (2016) 10–27.

[13] E. Yalcin, M. Can, C. Rodriguez-Seco, E. Aktas, R. Pudi, W. Cambarau, S. Demic, E. Palomares, Semiconductor self-assembled monolayers as selective contacts for efficient PiN perovskite solar cells, Energy Environ. Sci. 12 (2019) 230–237.

[14] D. Akın Kara, K. Kara, G. Oylumluoglu, M.Z. Yigit, M. Can, J.J. Kim, E.K. Burnett, D.L. Gonzalez Arellano, S.m. Buyukcelebi, F. Ozel, Enhanced device efficiency and long-term stability via boronic acid-based self-assembled monolayer modification of indium tin oxide in a planar perovskite solar cell, ACS Appl. Mater. Interfaces 10 (2018) 30000–30007.

[15] H. Kim, K.-G. Lim, T.-W. Lee, Planar heterojunction organometal halide perovskite solar cells: roles of interfacial layers, Energy Environ. Sci. 9 (2016) 12–30.

[16] W. Feng, S. Rangan, Y. Cao, E. Galoppini, R. Bartynski, E. Garfunkel, Energy level alignment of polythiophene/ZnO hybrid solar cells, J. Mater. Chem. 2 (2014) 7034–7044.

[17] M.C. Scharber, D. Mühlbacher, M. Koppe, P. Denk, C. Waldauf, A.J. Heeger, C. J. Brabec, Design rules for donors in bulk-heterojunction solar cells—towards 10% energy-conversion efficiency, Adv. Mater. 18 (2006) 789–794.

[18] H.L. Yip, S.K. Hau, N.S. Baek, H. Ma, A.K.Y. Jen, Polymer solar cells that use self-assembled-monolayer-modified ZnO/metals as cathodes, Adv. Mater. 20 (2008) 2376–2382.

[19] S. Khodabakhsh, B.M. Sanderson, J. Nelson, T.S. Jones, Using self-assembling dipole molecules to improve charge collection in molecular solar cells, Adv. Funct. Mater. 16 (2006) 95–100.

[20] N.H. Kim, G.W. Choi, Y.J. Seo, W.S. Lee, Indium tin oxide film characteristics after chemical mechanical polishing process with control of pad conditioning temperature, in: Solid State Phenomena, Trans Tech Publ, 2007, pp. 263–266.

[21] G. Liu, J.B. Kerr, S. Johnson, Dark spot formation relative to ITO surface roughness for polyfluorene devices, Synth. Met. 144 (2004) 1–6.

[22] D. Cheyns, J. Poortmans, P. Heremans, C. Deibel, S. Verlaak, B.P. Rand, J. Genoe, Analytical model for the open-circuit voltage and its associated resistance in organic planar heterojunction solar cells, Phys. Rev. B 77 (2008) 165332.

[23] R. Qiao, L. Zuo, Self-assembly monolayers boosting organic–inorganic halide perovskite solar cell performance, J. Mater. Res. 33 (2018) 387–400.

[24] L.S. Sapochak, A.B. Padmaperuma, X. Cai, J.L. Male, P.E. Burrows, Inductive effects of diphenylphosphoryl moieties on carbazole host materials: design rules for blue electrophosphorescent organic light-emitting devices, J. Phys. Chem. C 112 (2008) 7989–7996.

[25] H. Yan, P. Lee, N.R. Armstrong, A. Graham, G.A. Evmenenko, P. Dutta, T.J. Marks, High-performance hole-transport layers for polymer light-emitting diodes. Implementation of organosiloxane cross-linking chemistry in polymeric electroluminescent devices, J. Am. Chem. Soc. 127 (2005) 3172–3183.

[26] K. Wong, H. Yip, Y. Luo, K. Wong, W. Lau, K. Low, H. Chow, Z. Gao, W. Yeung, C. Chang, Blocking reactions between indium-tin oxide and poly (3, 4-ethylene dioxythiophene): poly (styrene sulphonate) with a self-assembly monolayer, Appl. Phys. Lett. 80 (2002) 2788–2790.

[27] M. De Jong, L. Van Ijzendoorn, M. De Voigt, Stability of the interface between indium-tin-oxide and poly (3, 4-ethylenedioxythiophene)/poly (styrenesulfonate) in polymer light-emitting diodes, Appl. Phys. Lett. 77 (2000) 2255–2257.

[28] M.Z.H. Khan, Effect of ITO surface properties on SAM modification: a review toward biosensor application, Cogent Eng 3 (2016), 1170097.

[29] S.A. Jadhav, Self-assembled monolayers (SAMs) of carboxylic acids: an overview, Cent. Eur. J. Chem. 9 (2011) 369–378.

[30] H. Alptekin, E. Arkan, C. Özbek, M. Can, A. Farzaneh, M. Sütçü, S. Okur, A. J. Cobley, Water affinity guided tunable superhydrophobicity and optimized wettability of selected natural minerals, J. Coating Technol. Res. 16 (2019) 199–211.

[31] H. Zhou, Q. Chen, G. Li, S. Luo, T.-b. Song, H.-S. Duan, Z. Hong, J. You, Y. Liu, Y. Yang, Interface engineering of highly efficient perovskite solar cells, Science 345 (2014) 542–546.

[32] R.N. Wenzel, Resistance of solid surfaces to wetting by water, Ind. Eng. Chem. 28 (1936) 988–994.

[33] M. Can, A.K. Havare, H. Aydın, N. Yagmurcukardes, S. Demic, S. Icli, S. Okur, Electrical properties of SAM-modified ITO surface using aromatic small molecules with double bond carboxylic acid groups for OLED applications, Appl. Surf. Sci. 314 (2014) 1082–1086.

[34] P. Prieto, V. Nistor, K. Nouneh, M. Oyama, M. Abd-Lefdil, R. Díaz, XPS study of silver, nickel and bimetallic silver–nickel nanoparticles prepared by seed-mediated growth, Appl. Surf. Sci. 258 (2012) 8807–8813.

[35] K.J. Carroll, J.U. Reveles, M.D. Shultz, S.N. Khanna, E.E. Carpenter, Preparation of elemental Cu and Ni nanoparticles by the polyol method: an experimental and theoretical approach, J. Phys. Chem. C 115 (2011) 2656–2664.

[36] E. Yalcin, D.A. Kara, C. Karakaya, M.Z. Yigit, A.K. Havare, M. Can, C. Tozlu, S. Demic, M. Kus, A. Aboulouard, Functionalized organic semiconductor molecules to enhance charge carrier injection in electroluminescent cell, Opt. Mater. 69 (2017) 283–290.

[37] F. Montagne, J. Polesel-Maris, R. Pugin, H. Heinzelmann, Poly (N-isopropylacrylamide) thin films densely grafted onto gold surface: preparation, characterization, and dynamic AFM study of temperature-induced chain conformational changes, Langmuir 25 (2008) 983–991.

[38] Z. Ahmad, M.A. Najeeb, R. Shakoor, A. Alashraf, S.A. Al-Muhtaseb, A. Soliman, M. Nazeeruddin, Instability in CH 3 NH 3 PbI 3 perovskite solar cells due to elemental migration and chemical composition changes, Sci. Rep. 7 (2017) 15406.

[39] G. Tai, T. Zeng, J. Yu, J. Zhou, Y. You, X. Wang, H. Wu, X. Sun, T. Hu, W. Guo, Fast and large-area growth of uniform MoS 2 monolayers on molybdenum foils, Nanoscale 8 (2016) 2234–2241.

[40] R. Xu, L. Xiao, L. Luo, Q. Yuan, D. Qin, G. Hu, W. Gan, Nitrogen, sulfur dual-doped mesoporous carbon modified glassy carbon electrode for simultaneous determination of hydroquinone and catechol, J. Electrochem. Soc. 163 (2016) B617–B623.

[41] J. Yu, X. Chen, Y. Wang, H. Zhou, M. Xue, Y. Xu, Z. Li, C. Ye, J. Zhang, P.A. Van Aken, A high-performance self-powered broadband photodetector based on a CH 3 NH 3 PbI 3 perovskite/ZnO nanorod array heterostructure, J. Mater. Chem. C 4 (2016) 7302–7308.

[42] X. Zou, H. Fan, Y. Tian, S. Yan, Synthesis of Cu 2 O/ZnO hetero-nanorod arrays with enhanced visible light-driven photocatalytic activity, CrystEngComm 16 (2014) 1149–1156.

[43] X. Fan, C. Cui, G. Fang, J. Wang, S. Li, F. Cheng, H. Long, Y. Li, Efficient polymer solar cells based on poly (3-hexylthiophene): indene-C70 bisadduct with a MoO3 buffer layer, Adv. Funct. Mater. 22 (2012) 585–590.

[44] J.H. Heo, S.H. Im, J.H. Noh, T.N. Mandal, C.-S. Lim, J.A. Chang, Y.H. Lee, H.-j. Kim, A. Sarkar, M.K. Nazeeruddin, Efficient inorganic–organic hybrid heterojunction solar cells containing perovskite compound and polymeric hole conductors, Nat. Photon. 7 (2013) 486.

[45] X. Guo, C. McCleese, C. Kolodziej, A.C. Samia, Y. Zhao, C. Burda, Identification and characterization of the intermediate phase in hybrid organic–inorganic MAPbI 3 perovskite, Dalton Trans. 45 (2016) 3806–3813.

[46] Y. Li, Y. Zhao, Q. Chen, Y. Yang, Y. Liu, Z. Hong, Z. Liu, Y.-T. Hsieh, L. Meng, Y. Li, Multifunctional fullerene derivative for interface engineering in perovskite solar cells, J. Am. Chem. Soc. 137 (2015) 15540–15547.

[47] A.P. Hinckley, A.J. Muscat, Detecting and removing defects in organosilane self-assembled monolayers, Langmuir 36 (2020) 2563–2573.

[48] X.-M. Zhao, J.L. Wilbur, G.M. Whitesides, Using two-stage chemical amplification to determine the density of defects in self-assembled monolayers of alkanethiolates on gold, Langmuir 12 (1996) 3257–3264.

[49] M. Chockalingam, N. Darwish, G. Le Saux, J.J. Gooding, Importance of the indium tin oxide substrate on the quality of self-assembled monolayers formed from organophosphonic acids, Langmuir 27 (2011) 2545–2552.

[50] T. Ishida, H. Kobayashi, Y. Nakato, Structures and properties of electron-beam-evaporated indium tin oxide films as studied by X-ray photoelectron spectroscopy and work-function measurements, J. Appl. Phys. 73 (1993) 4344–4350.

[51] D. Głowienka, D. Zhang, F. Di Giacomo, M. Najafi, S. Veenstra, J. Szmytkowski, Y. Galagan, Role of surface recombination in perovskite solar cells at the interface of HTL/CH3NH3PbI3, Nano. Energy 67 (2020) 104186.

[52] G. Landi, C. Barone, A. De Sio, S. Pagano, H. Neitzert, Characterization of polymer: fullerene solar cells by low-frequency noise spectroscopy, Appl. Phys. Lett. 102 (2013) 223902.

[53] G. Landi, H.C. Neitzert, C. Barone, C. Mauro, F. Lang, S. Albrecht, B. Rech, S. Pagano, Correlation between electronic defect states distribution and device performance of perovskite solar cells, Adv Sci 4 (2017) 1700183.

[54] H.J. Snaith, A. Abate, J.M. Ball, G.E. Eperon, T. Leijtens, N.K. Noel, S.D. Stranks, J. T.-W. Wang, K. Wojciechowski, W. Zhang, Anomalous hysteresis in perovskite solar cells, J. Phys. Chem. Lett. 5 (2014) 1511–1515.

[55] L. Zuo, Q. Chen, N. De Marco, Y.-T. Hsieh, H. Chen, P. Sun, S.-Y. Chang, H. Zhao, S. Dong, Y. Yang, Tailoring the interfacial chemical interaction for high-efficiency perovskite solar cells, Nano Lett. 17 (2016) 269–275.